A snapshot of internal waves and hydrodynamic instabilities in the Southern Bay of Bengal

8 authors, including:

Iossif Lozovatsky
University of Notre Dame
73 PUBLICATIONS **1,227** CITATIONS

Hemantha Wijesekera
United States Navy
91 PUBLICATIONS **1,655** CITATIONS

M.-J. Lilover
Tallinn University of Technology
62 PUBLICATIONS **452** CITATIONS

Annunziata Pirro
National Institute of Oceanography and Applied Geophysics - OGS
12 PUBLICATIONS **127** CITATIONS

A snapshot of internal waves and hydrodynamic instabilities in the southern Bay of Bengal

Iossif Lozovatsky[1], Hemantha Wijesekera[2], Ewa Jarosz[2], Madis-Jaak Lilover[3], Annunziata Pirro[1], Zachariah Silver[1], Luca Centurioni[4], and H. J. S. Fernando[1,5]

[1]Department of Civil and Environmental Engineering and Earth Sciences, University of Notre Dame, Notre Dame, Indiana, USA, [2]Naval Research Laboratory, Stennis Space Center, Mississippi, USA, [3]Institute of Marine Systems, Tallinn University of Technology, Tallinn, Estonia, [4]Scripps Institution of Oceanography, University of California, San Diego, La Jolla, CA, USA, [5]Department of Aerospace and Mechanical Engineering, University of Notre Dame, Notre Dame, Indiana, USA

Abstract Measurements conducted in the southern Bay of Bengal (BoB) as a part of the ASIRI-EBoB Program portray the characteristics of high-frequency internal waves in the upper pycnocline as well as the velocity structure with episodic events of shear instability. A 20 h time series of CTD, ADCP, and acoustic backscatter profiles down to 150 m as well as temporal CTD measurements in the pycnocline at $z = 54$ m were taken to the east of Sri Lanka. Internal waves of periods $\sim$10–40 min were recorded at all depths below a shallow ($\sim$20–30 m) surface mixed layer in the background of an 8 m amplitude internal tide. The absolute values of vertical displacements associated with high-frequency waves followed the Nakagami distribution with a median value of 2.1 m and a 95% quantile 6.5 m. The internal wave amplitudes are normally distributed. The tails of the distribution deviate from normality due to episodic high-amplitude displacements. The sporadic appearance of internal waves with amplitudes exceeding $\sim$5 m usually coincided with patches of low Richardson numbers, pointing to local shear instability as a possible mechanism of internal-wave-induced turbulence. The probability of shear instability in the summer BoB pycnocline based on an exponential distribution of the inverse Richardson number, however, appears to be relatively low, not exceeding 4% for $Ri < 0.25$ and about 10% for $Ri < 0.36$ (K-H billows). The probability of the generation of asymmetric breaking internal waves and Holmboe instabilities is above $\sim$25%.

1. Introduction

Numerical modeling of the water exchange between the Arabian Sea (AS) and the Bay of Bengal (BoB) [*Vinayachandran and Yamagata*, 1998; *Jensen*, 2001; *de Vos et al.*, 2014] suggests that high winds with positive wind stress curl during the southwestern monsoon induce mixing of saltier AS water with fresher water from the BoB. This mostly happens between 5°N–10°N and 82°E–88°E. Profiles of temperature and salinity collected in 2009 in the southern BoB [*Vinayachandran et al.*, 2013], where upward pumping of saltier water has been observed during the summer monsoon (July–August), support this notion. It is also assumed that these mixed water masses are further advected into the central and northern BoB by currents and mesoscale eddies. Lesser known, however, is the role of submesoscale processes such as internal waves in generating and sustaining diapycnal mixing between the AS and the BoB waters, due mainly to the lack of in situ high-resolution measurements in the southern BoB.

To fill this gap, an array of six moorings was deployed in December 2013 to collect long-term (more than a year and a half) oceanographic data throughout the upper 450 m of the water column, supplemented by the first detailed ADCP survey in the southern BoB [*Wijesekera et al.*, 2015]. In July 2014, a series of high-spatial-resolution sections of CTD (ScanFish) and ADCP measurements were carried out in the mooring region, between 5°15′–8°12′N and 85°15′–86°25′E, to quantify advection and mixing associated with the Summer Monsoon Current, freshwater-saltwater exchanges, and internal wave forcing.

Allusion to internal waves in the Indian Ocean dates back to the mid-nineteenth century [*Maury*, 1861]. Internal waves in the BoB are affected by the rough bathymetry, seasonal wind forcing, and strong stratification, which govern both the generation and breakdown of internal waves. In particular, the generation of internal waves due to interaction of barotropic tide with bathymetry has been reported over shallow gaps between Andaman and

Nicobar Islands [e.g., *Jackson*, 2004; *Osborne and Burch*, 1980]. In the Andaman Sea, nonlinear internal waves (NLIW) are extremely large, with amplitude >60 m, wavelengths ∼6–15 km, and phase speed >2 m/s [*Osborne and Burch*, 1980]. Although satellite imagery shows the propagation of NLIW across the BoB toward Sri Lanka and their thronging along the continental shelf of India [*Jackson*, 2009], NLIW to the west of Andaman and Nicobar Islands remains largely unexplored. Recently, NLIW observations from SAR images have been reported in the northern BoB [*Rao et al.*, 2010; *Prasad and Rajasekhar*, 2011]. These waves propagated toward the Indian coast with wavelengths ∼600–700 m. On the Indian shelf of the northern BoB, semidiurnal tidal internal waves were characterized by amplitudes of ∼7 m, the amplitude of the diurnal internal tide being about half of it [*Sridevi et al.*, 2010]. In the coastal waters of Sri Lanka, *Wijeratne et al.* [2010] observed internal seiches with periods up to 2 h, with the largest amplitudes occurring in the transition period between spring and neap tides, which was attributed to internal waves originating as far away as the Andaman Islands and traveling to the eastern coast of Sri Lanka over 6–8 days. There have been no in situ measurements of internal waves in the BoB blue water until recently [*Lucas et al.*, 2014].

The upper ocean mixing in the BoB under various wind conditions has not been studied in detail. Strong shears of monsoon driven currents can enhance internal-wave-driven mixing on diurnal time scales, similar to that observed during TOGA-COARE [*Smyth et al.*, 1997; *Wijesekera and Gregg*, 1996]. Detailed studies in the area, including internal waves and fine structure measurements, are required for better understanding of coupled ocean-atmosphere processes. The latest measurements in the southern BoB conducted in July 2014 described in this paper shed light on basic characteristics of high-frequency internal waves in the upper pycnocline as well as episodic events of shear instability.

2. Measurements and Data Processing

On 7–8 July 2014, an opportunistic 20 h experiment was conducted at a fixed point in the southern Bay of Bengal, focusing on internal waves and shear instability in the pycnocline and small-scale dynamics of the surface layer. The cruise in point was a part of the collaborative ASIRI-EBoB project focused on small scale to mesoscale variability in the southern BoB during the summer monsoon. Time series of currents and hydrographic profiles were collected from the R/V Roger Revelle while the ship maintained a permanent position at the station $\varphi = 8°07.2'$N, $\lambda = 85°21.5'$E (a red filled circle in Figures 1a and 1b) to the north of a large pool of enhanced sea surface chlorophyll concentration (green-yellow patch between ∼6°N–7°N and 84.5°E–86.5°E), which is due to a phytoplankton bloom following the upwelling of nutrient-rich deeper waters. Conceivably, this upwelling is a result of Ekman pumping associated with the Sri Lanka Dome (SLD) [*Anil Kumar*, 2015]. The CTD measurements were taken every 30 min down to 150 m using a Seabird 911*plus* vertical profiler. Between each cast, the instrument sojourned in the pycnocline for about 25 min at the reference depth $z_0 = 54$ m. As a result, 41 vertical profiles of temperature $T(t, z)$, salinity $S(t, z)$, and potential density $\rho_\theta(t, z)$ as well as 40 time records of $T_i(t, z_0)$, $S_i(t, z_0)$, and $\rho_{\theta_i}(t, z_0)$ were obtained. Here t is the time and z is positive downward. In parallel, standard shipboard meteorological measurements (Figure 2) as well as profiling of zonal $u(z, t)$ and meridional $v(z, t)$ components of horizontal velocity were made using ship-mounted 150 kHz Acoustic Current Doppler Profiler (ADCP) and 140 kHz Hydrographic Doppler Sonar System (HDSS) [see *Pinkel et al.*, 2003]. The acoustic backscatter profiles obtained in the upper 150 m using 123 kHz Biosonics DTX Echo Sounder (sampling rate 1.5 Hz) supplemented the CTD time records, allowing the analysis of internal waves not only at $z_0 = 54$ m but also at the other depths in the pycnocline.

The Seabird CTD profiling data (24 Hz sampling rate) were averaged and interpolated to obtain $T(z)$, $S(z)$, and $\rho_\theta(z)$ profiles with a fine-scale resolution of $\Delta z = 2$ m as well as 3 m to match the resolution of HDSS for calculating the Richardson numbers. The original time records at z_0 were low-pass filtered and averaged to eliminate the noise induced by pitch and roll of the ship. The time step Δt for processed $T(t, z_0)$, $S(t, z_0)$, and $\rho_\theta(t, z_0)$ series is 20 s.

The biosonic hydroacoustic data were analyzed using Sonar5-Pro Post Processing System [e.g., *BioSonics*, 2004; *Depew et al.*, 2009; *Balk and Lindem*, 2007; *Rudstam et al.*, 2009]. The data down to 2.5 m depth were excluded to eliminate the near-field and surface noise of transducers. The acoustic signal was filtered and averaged in time and over the depth. The resulting matrix contained 16 h of profiles from 2.5 to 149.5 m with $\Delta z = 1$ m and $\Delta t = 30$ s (the first 4 h of the measurements are excluded due to sporadic interruption of the data recording).
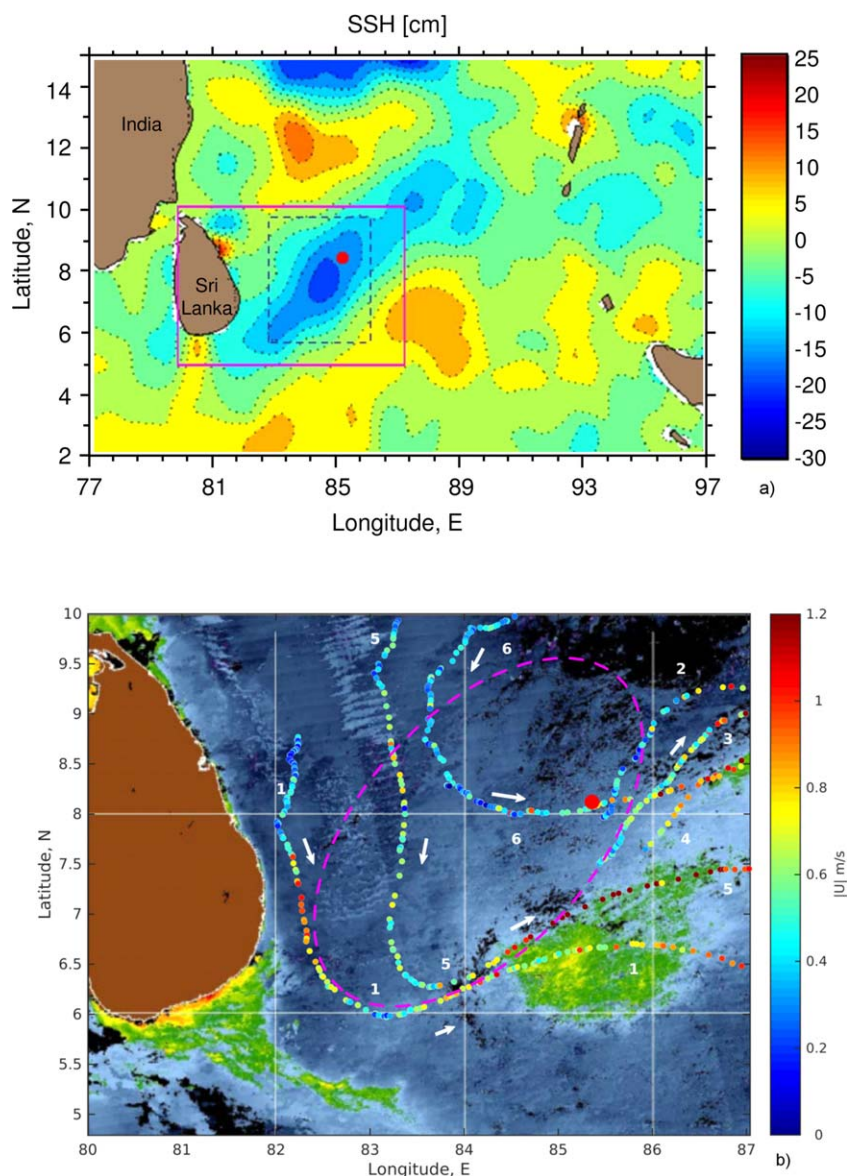
Figure 1. (a) The real-time mesoscale altimetry (SSH, sea surface height) of the Bay of Bengal for 8 July 2014 (Colorado Center for Astrodynamics Research, University of Colorado at Boulder (CO CCAR), http://eddy.colorado.edu/ccar/ssh/nrt_global_grid_viewer). The Sri Lankan Dome is a large cyclonic eddy encircled by the blue dashed square. It is neighbored by a large anticyclonic feature to the southeast (the orange-colored area between 4.5°N–7.5°N and 85.9°E–89.5°E). The sampling site is shown by a red circle at the northeastern periphery of the SLD. The magenta rectangle indicates boundaries of the ocean color map given in Figure 1b. (b) The weakly composite (30 June–3 July) image of the BoB ocean color, showing enhanced chlorophyll concentration (green regions) associated with a phytoplankton bloom. The red circle at 8°7.2′N, 85°21.5′E is the site of the 20 h profiling series. Directions (white arrows) and velocities (color pallet) of six drifters are shown along their trajectories. The parameters of the drifts are in Table 1. The magenta dashed ellipse indicates a region occupied by the SLD in June–July 2014.

The 150 kHz ADCP data were collected between 21 and 141 m, with temporal and vertical resolutions of 3 min and 8 m, respectively. The 140 kHz HDSS profiler provided data with a finer vertical ($\Delta z = 3$ m in the depth range between 19 and 150 m) and temporal (1 min, averaging over 100 pings) resolutions [*Rainville and Pinkel*, 2004].

3. Background Meteorological Conditions, Stratification, and Currents

3.1. Atmospheric Conditions and Surface Currents

To quantify atmospheric conditions for the period of our multicast measurements, the shipboard wind speed $W_a(t)$ and direction $\phi_a(t)$, air temperature $T_a(t)$ and humidity $r_a(t)$), the near-surface ($z = 5$ m) water
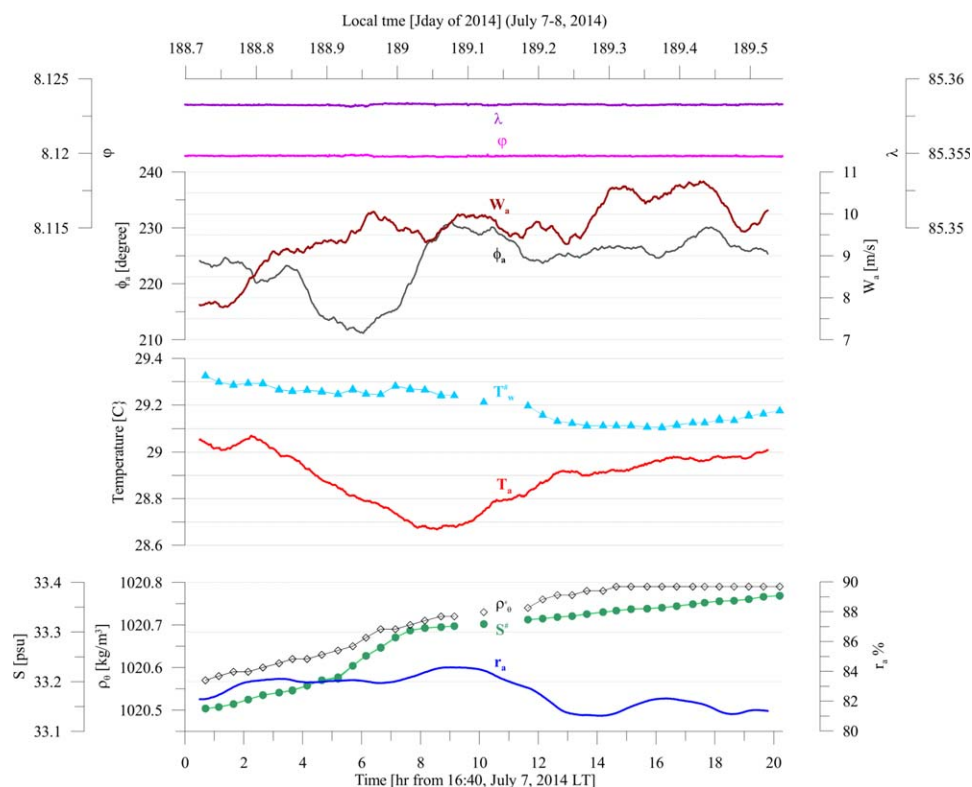
Figure 2. Latitude φ and longitude λ of the measurement site, wind speed W_a and wind direction ϕ_a, air temperature T_a, and relative humidity r at 17 m above the sea surface. The Seabird near-surface ($z = 5$ m) water temperature $T_w^\#$, salinity $S^\#$, and potential density $\rho_\theta^\#$ during 20 h of CTD measurements.

temperature $T_w^\#(t)$, salinity $S^\#(t)$, and potential density $\rho_\theta^\#(t)$ as well as the ship latitude and longitude are shown in Figure 2. It is evident that persistent southwest monsoons (moderate winds of 8–11 m/s from the southwest; $\phi_a = 210$–$225°$) prevailed in the region. The amplitude of the diurnal air temperature cycle at the measurement site was small $\sim 0.4°C$, and the temperature minimum $T_a^{min} \sim 28.7°C$ was observed just after midnight of the local time (LT). The sea-surface water temperature $T_w^\#(t)$ did not follow $T_a(t)$, decreasing from 29.32°C at 17:00 on 7 July to 29.1°C at $\sim$6 A.M. on 8 July, and then it began slowly rising after 10 A.M. It seems that $T_w^\#(t)$ was more affected by horizontal advection than by air-sea interactions. This is in agreement with the continuous increase of near-surface salinity $S^\#(t)$ and potential density $\rho_\theta^\#(t)$ in Figure 2.

The barotropic tidal currents and surface elevations in the region are shown in Figure 3. The meridional barotropic component v_{BT} was dominated by the M2 constituent with an amplitude of ~ 2.5 cm/s, and the zonal component u_{BT} was as equally influenced by M2 and K1 constituents (not shown here) having a much smaller amplitude (~ 0.5 cm/s) than v_{BT}. As a result, the tidal ellipses (Figure 3a) are complex, stretching substantially in the north-south direction. The tidal surface elevation did not exceed 25 cm. The calculations were made using thirteen tidal constituents available from the OSU TOPEX/Poseidon ATLAS Global and Regional Solutions [*Egbert and Erofeeva*, 2002, http://volkov.oce.orst.edu/tides/atlas.html]

The transport of more saline, slightly cooler, waters in the surface layer can be linked to the circulation associated with the SLD (and also to upwelling and mixing) that developed in the region toward the end of June in response to cyclonic wind stress curl in the regional wind field [*Vinayachandran and Yamagata*, 1998]. At the beginning of July 2014, the SLD stretched along its longer northeastern-southwestern axis, at the same time moving slightly to the west. This notion is based on the analysis of maps of the sea surface height (SSH) retrieved from AVISO archive (http://eddy.colorado.edu/ccar/ssh/nrt_global_grid_viewer) for the period between May and September of 2014. It appeared that the SLD originated at the end of May, fully developed in the second part of June, began spreading and moving slightly westward in late June,
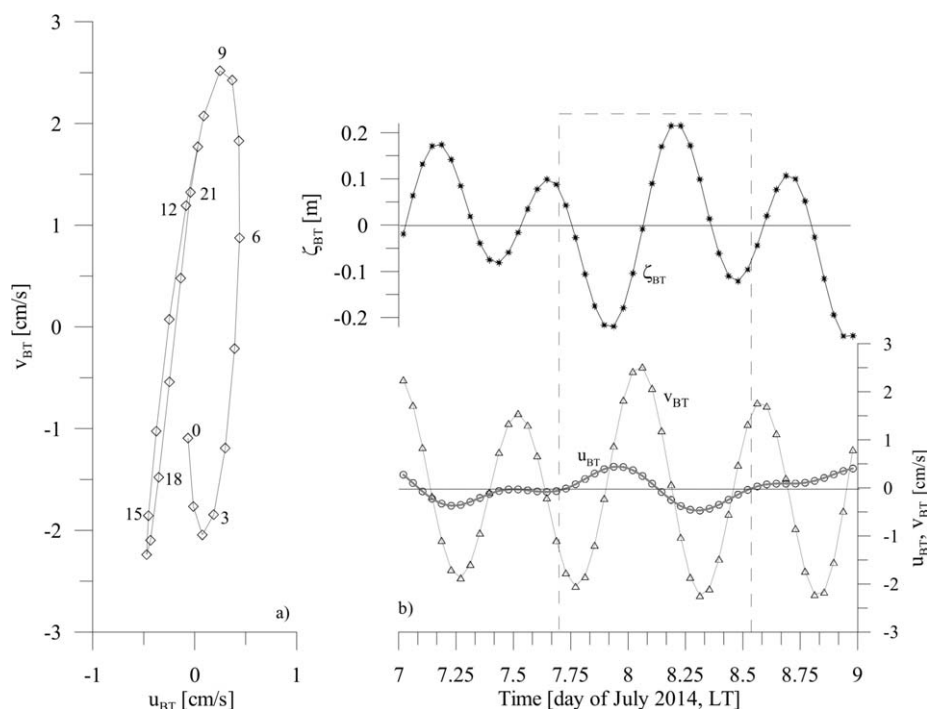
Figure 3. (a) Barotropic tidal ellipses based on 20 h of measurements at the location (the numbers near the symbols are hours from the beginning of observations); (b) zonal $u_{BT}(t)$ and meridional $v_{BT}(t)$ velocity components and surface elevation $\varsigma_{BT}(t)$ for 7–9 July 2014. The dashed box encompasses the observational period.

reflected from the Sri Lanka coast as it moves northeastward in July, and completely disappeared from its original position by the beginning of August. The 8 July SSH map is shown in Figure 1a. The measurement site was located presumably at the northeastern periphery of the cold SLD.

The trajectories of several surface floats, which drifted in the SLD region in late May–early August, support this concept (see Figure 1b). The drifters, with drogues centered at 15 m below the sea surface [*Lumpkin and Pazos*, 2007] were launched in the BoB within the framework of the ASIRI program (H. W. Wijesekera et al., ASIRI: An ocean-atmosphere initiative for Bay of Bengal, submitted to *Bulletin of the American Meteorological Society*, 2016). In June, the maximum curvature of the drifter #1 trajectory and the high speed of the counterclockwise-rotated surface current were observed at ∼6°N, 83.2°E. In July, another drifter (#5) depicted a similar trajectory, but with the maximum curvature shifted to the northeast (∼6.3°N, 83.6°E). In late July (drifter #6), the counterclockwise rotation with a substantially lower speed was observed much further to the northwest. Starting approximately at 8°N/85.5°E, drifter #6 as well as drifters #2, #3, and #4, which were launched in early July approximately in the same region (see Figure 1b and Table 1), moved to the northeast and then further to the east rather than drifting to the north and northwest, as expected by anticyclonic SLD circulation. Drifters #1 and #5 also left the anticyclonic circulation to the east of ∼85.5°E and were affected by a large anticyclonic feature located southeast of SLD (the yellow-colored area between 4.5°N–7.5°N and 85.9°E–88.5°E in Figure 1a). The upwelling-favorable divergence frontal zone between the colder SLD and the neighboring warmer anticyclonic feature appears to supply nutrients to the sea surface, inducing a high chlorophyll concentration observed in the region (Figure 1b). Note that the

Table 1. Characteristics of the Drifter Trajectories Shown in Figure 1b

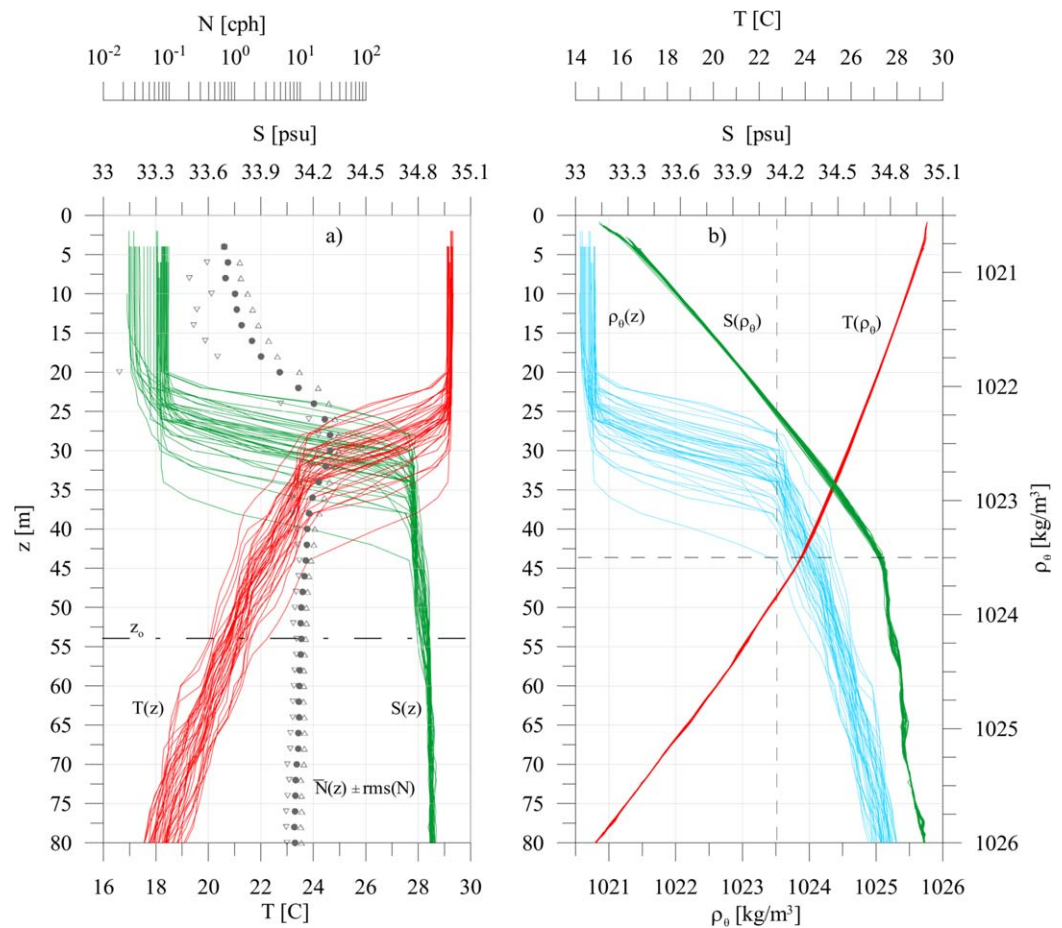| Drifter Number	Start Time	End Time	Drift Duration (Days)	Drift Distance (km)	Average Velocity (m/s)
1	23 May, 04:00	9 Jun, 04:00	17	840.3	0.57
2	3 Jul, 16:00	10 Jul, 04:00	9.5	251.5	0.42
3	3 Jul, 21:00	9 Jul, 15:00	5.75	254.8	0.56
4	6 Jul, 23:15	9 Jul, 15:00	2.63	154.4	0.89
5	6 Jul, 20:30	20 Jul, 23:15	14.12	848.4	0.68
6	16 Jul, 16:30	2 Aug, 08:00	17	646.1	0.44

Figure 4. Temperature $T(z)$, salinity $S(z)$, and the ensemble-averaged buoyancy frequency $\bar{N}(z) \pm rms(N)$ profiles in the upper 80 m (a) and profiles of potential density $\rho_\theta(z)$, $T(\rho_\theta)$, and $S(\rho_\theta)$ in the same depth range; z_0 is the depth of CTD time records, the dashed lines in the right figure indicate the lowest boundary of a sharp pycnocline at $\rho_\theta = 1023.5$ kg/m^3.

approximate realm of SLD in June–July of 2014 is indicated by a dashed magenta line depicted in Figure 1b.

3.2. Stratification

All 41 profiles of $T(z)$, $S(z)$, and $\rho_\theta(z)$ obtained during the fixed-point Seabird measurements as well as the calculated ensemble-averaged buoyancy frequency profiles with the rms limits $\bar{N}(z) \pm rms(N)$ are shown in Figure 4 for the upper 80 m. From 80 to 150 m, the temperature continuously decreased with depth with the mean (overbar) gradient of $\frac{\Delta \bar{T}}{\Delta z}_{(150-80)} = -(5.1-5.5) \times 10^{-2}$°C/m). $\bar{N}(z)$ also decreased from ~9 to ~5 cph, while there was an increase in salinity and potential density and their mean gradients were $\frac{\Delta \bar{S}}{\Delta z}_{(150-80)} = (1.71-1.77) \times 10^{-3}$ psu/m and $\frac{\Delta \bar{\rho}_\theta}{\Delta z}_{(150-80)} = (1.29-1.46) \times 10^{-2}$ kg/m^4, respectively. The region below the upper mixed layer was conducive to internal-wave perturbations, causing a relatively wide scatter of the thermohaline profiles (Figure 4a). This scatter essentially vanished when T and S are plotted against the potential density. Figure 4b shows the collapse of $T(\rho_\theta)$ and $S(\rho_\theta)$. Under moderate winds, the lower boundary of the sharp density interface z_{plb} (marked by dashed lines in Figure 4b) is expected to be almost unaffected by surface fluxes. Thus, the variations of z_{plb} can provide an estimate of the height η_{lf} of low-frequency linear internal waves, which heaves the entire pycnocline. It is shown in Figure 4b that z_{plb} varies between 27 and 43 m, leading to $\eta_{lf} \approx 16$ m.

During the observational period, the surface mixed-layer depth (MLD) varied from ~19 to 33 m (Figure 4). The MLD was estimated visually using the density profiles. Figure 5 shows that the MLD was influenced by air-sea interactions (the deepest MLD was observed in the early morning of 8 July) as well as by higher-
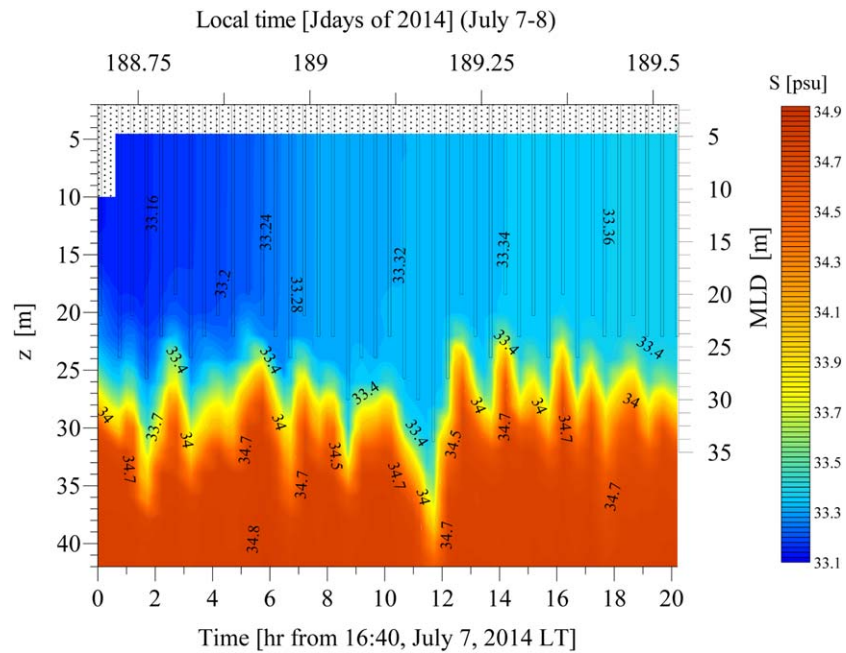
Figure 5. Salinity in the upper 42 m layer (colored contour plot) and the mixed-layer depth (bars) at the test site in the southern BoB.

frequency internal waves present in the underlying narrow pycnocline. Quasiperiodic oscillations of the MLD (Figure 5) are well correlated with the internal-wave displacements of the halocline, specifically during the daytime where the sea surface fluxes do not change much. The advection of higher saline waters near the sea surface by the northeasterly directed currents from the southwest was spread over the entire mixed layer (Figure 5), indicating that surface layer currents occupied the entire upper quasi-homogeneous layer, but whether they also penetrated the pycnocline can be explored using our ADCP data.
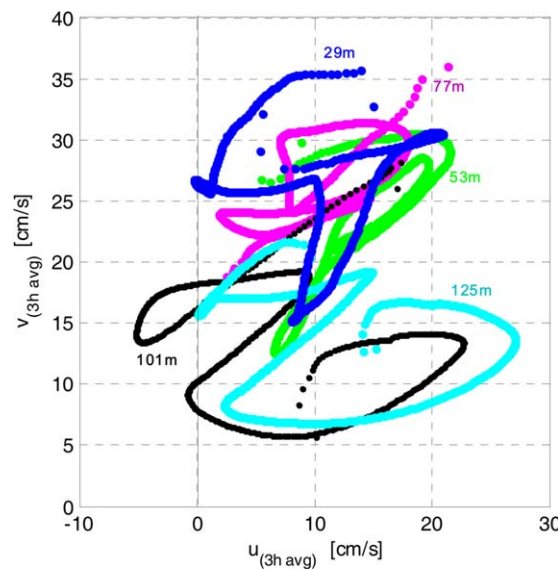

Figure 6. Low-frequency currents (after a running average equivalent to ~3 h) at several depth levels in the pycnocline are indicated in the plot.

3.3. Currents in the Pycnocline
Complex nature of currents at the site (those, which are not affected by high-frequency oscillations) is exemplified by irregular semienclosed loops shown in Figure 6 for several characteristic depths in the pycnocline: $z = 29, 53, 77, 101$, and 125 m. Note the velocity components in Figure 6 were presmoothed over 60 points by run-averaging filter (eliminating fluctuations with the periods less than ~3 h). Note that the mesoscale circulation associated with the SLD as well as baroclinic tidal motions could be present simultaneously. The latter is supported by the depth averaged ($Dz = 21–141$ m) zonal and meridional components $u_{avr}(t)$ and $v_{avr}(t)$ that are overlaid in the corresponding upper and middle panels in Figure 7 and were fitted by a combination of two major tidal components, M2 and K1, in the region.

The depth-time variation of zonal $u(z, t)$ and meridional $v(z, t)$ velocity components and the
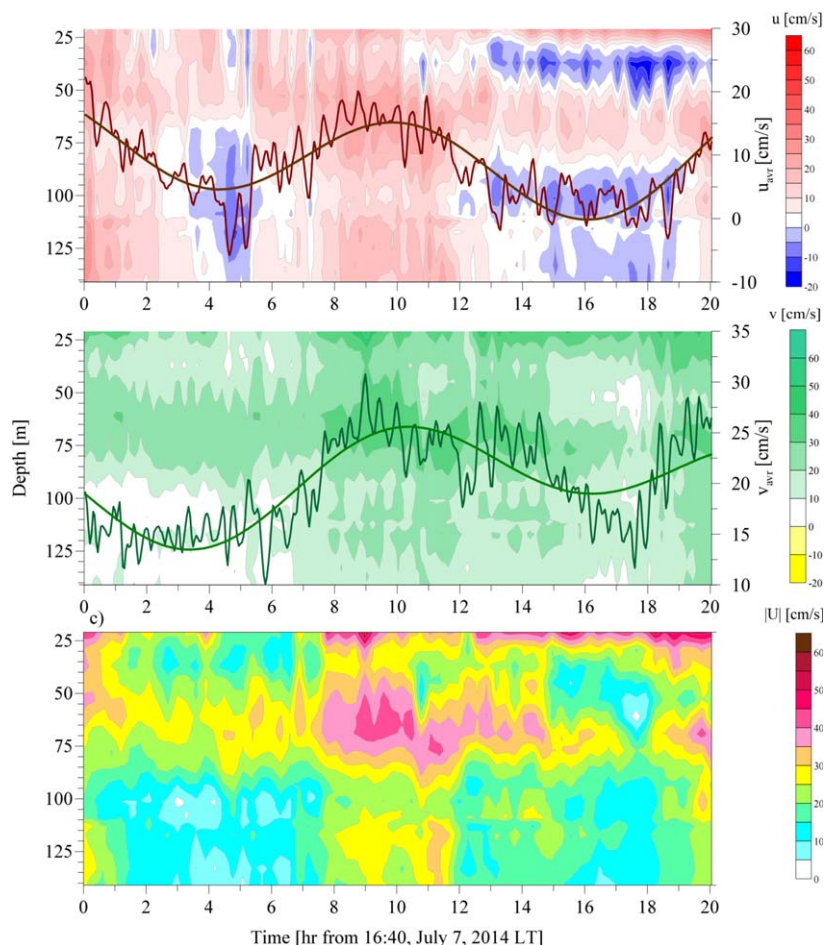
Figure 7. Contour plots of zonal $u(z, t)$ (upper) and meridional $v(z, t)$ (middle) velocity components and the velocity magnitude $|U|(z, t)$ (bottom) during the 20 h of CTD measurements. The depth-averaged (between $z = 21$ and 141 m) velocities $u_{avr}(t)$ and $v_{avr}(t)$ in the upper two panels were fitted by a combination of M2 and K1 tidal constituents.

velocity magnitude $|U|(z, t)$ suggest a clear multilayered structure of mean currents (Figure 7). It seems that the strong northeastward surface current identified by drifter trajectories in Figure 1b is confined to the upper mixed layer (above $\sim z \approx 20$–25 m), which is especially true for the second half of the observational period (depicted by red and green colors in this depth range in the $u(z, t)$ and $v(z, t)$ panels of Figure 7, respectively). Note that the barotropic tidal current is less than 3 cm/s (see Figure 3). In the narrow upper pycnocline ($Dz \approx 25$–40 m), the current magnitude is much weaker ($|U| \sim 10$ cm/s) than above the MLD. The flow even exhibits a westward velocity after $t \sim 12$ h (blue zone in Figure 7c), and it continues to be influenced by anticyclonic circulation of the SLD. The upper part of the main pycnocline ($Dz \sim 45$–80 m) is occupied by the strongest northeastward flow ($|U| \sim 25$–35 cm/s), with a maximum speed observed around $t \sim 9$–10 h. Below ~ 80 m, the northward flow is weaker ($|U| \sim 10$–15 cm/s), often showing westward (anticyclonic) component in the second half of the measurement period (the blue colored segments in Figures 7a and 7c). This supports the notion that the largest vertical displacement of the sharp density interface is induced by tidal internal waves, as noted by *Sridevi et al.* [2014]. However, the most eye-catching feature in Figure 7 is the well-identified higher-frequency oscillations of $u_{avr}(t)$ and $v_{avr}(t)$, which could be of internal-wave origin and will be discussed next.

4. Internal Waves

4.1. Velocity Spectra

The velocity oscillations in the pycnocline can be identified by calculating the variance preserving spectra of the kinetic energy $fS_{KE}(\log_{10} f) = 0.5f(S_u + S_v)$, which are shown in Figure 8a for several representative
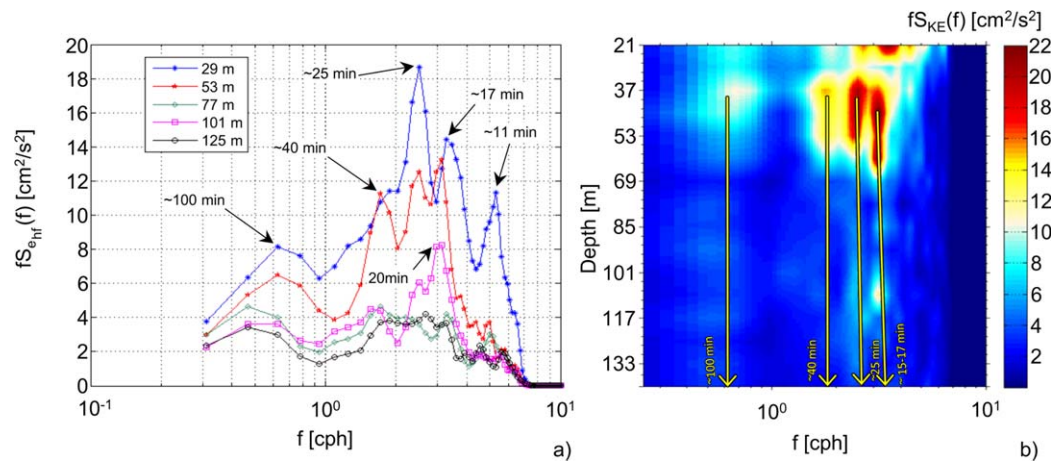
Figure 8. (a) The variance preserving spectra $fS_{e_{hf}}$ ($\log_{10} f$) of horizontal kinetic energy for frequencies (f) > ~0.3 cph occupied by internal waves (the major spectral maxima are labeled in minutes). The central depths z_i of the ADCP bins are in the legend. The characteristic buoyancy periods $\tau_N(z_i) = 2\pi/N_i$ at z_i = 29, 53, 77, 101, and 125 m are 2.1, 5.8, 7.1, 9.4, and 9.1 min, respectively. (b) The spectral section of the kinetic energy $fS_{KE}(f,z)$ of the high-frequency (periods from ~2 h to 9 min) velocity components in the pycnocline. The major spectral maxima are indicated by arrows. Periods of oscillations are in minutes.

depths (z = 29 m—a very sharp upper pycnocline; z = 53 m—the closest depth to the CTD time records; z = 77, 101, and 125 m—in the middle and close to the maximum depth of the profiles). The characteristic buoyancy periods $\tau_N(z_i) = 2\pi/N_i$ at z_i = 29, 53, 77, 101, and 125 m are 2.1, 5.8, 7.1, 9.4, and 9.1 min, respectively. The spectral densities S_u and S_v were calculated using the horizontal velocity components $u_{hf}(t,z)$ and $v_{hf}(t,z)$ (3 min sampling rate), which were slightly smoothed (3-point moving-average) and then high-pass filtered (60 points) to remove trends and oscillations with periods larger than ~3 h. A generalized view of the spectral structure of kinetic energy in the pycnocline is given in Figure 8b, highlighting the concentration of energy in several specific frequency bands above $z \sim 75$ m.

At the same time, the spectral maxima at $f^{-1} \equiv \tau \sim$ 17–19 min and $\tau \sim$ 24–25 min can be traced in Figure 8b down to at least 140 m, indicating dominant leaky modes below the base of the pycnocline determined by the strongly energetic nature of the corresponding frequencies in the pycnocline. Note that a slight change in frequency of several spectral maxima with depth could be caused by the Doppler shift due to the variability of the mean currents. The fS_{KE} spectra also displays statistically significant maxima at smaller, τ = 11–13 min, and larger, τ = 32–40 min, periods (Figure 8a). Relatively long-period oscillations ($\tau \sim$ 95–100 min) are identifiable almost at all depths in the pycnocline (peaking at ~z = 40 m), but with lower statistical confidence.

The integrated energy per unit mass of higher-frequency velocity components $e_{hf}(z,t) = 0.5\left[\langle u_{hf}^2 \rangle_{1.5hr} + \langle v_{hf}^2 \rangle_{1.5hr}\right]$ was calculated at consecutive 1.5 h long segments, and the corresponding contour plot is shown in Figure 9 (color palette in right panel) along with the average over the entire 20 h sampling period $\langle e_{hf} \rangle$
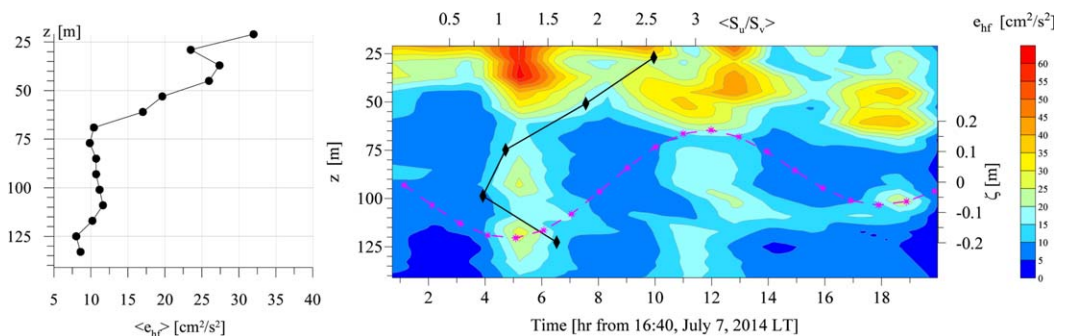
Figure 9. The energy of high-frequency current components $e_{hf}(z,t)$ averaged at 1.5 h consecutive time intervals (right) and the same variable $\langle e_{hf} \rangle$ averaged for the entire 20 h sampling period (left). The ratio between high-frequency-averaged spectra $\langle S_u/S_v \rangle$ of zonal and meridional components (black diamond line) and the tidal surface elevation $\zeta(t)$ (dotted magenta line) are shown in the right panel.
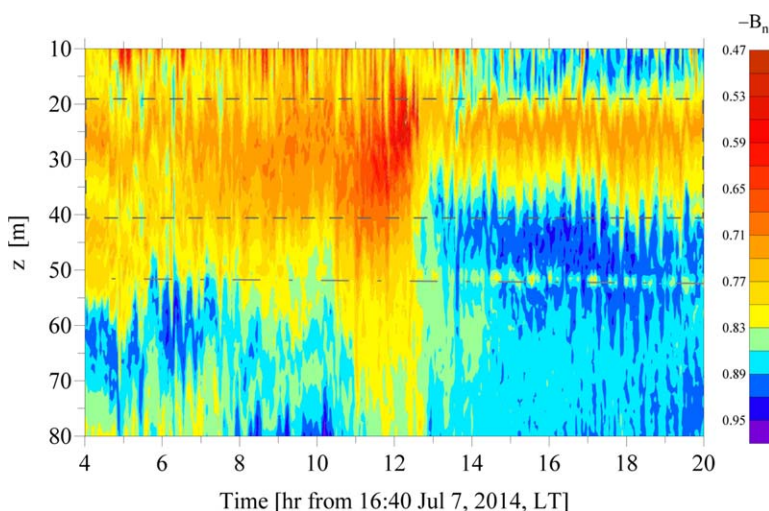
Figure 10. The normalized backscatter signal $-B_n = Bs/(-Bs_{max})$ (warmer colors are associated with higher strength) during 16 h of continuous operation at the measurement site. The dashed lines indicate the depth range occupied by a sharp density interface (see Figure 4); the dash-dotted line crossing through small lighter patches at $z = 53$–54 m resulting from backscatter amplification caused by the CTD profiler during times when 25 min time series were recorded at the fixed depth.

$(z) = 0.5 \left[\langle u^2(z) \rangle_{20hr} + \langle v^2(z) \rangle_{20hr} \right]$ (left panel). The figure depicts not only a substantial decrease of $\langle e_{hf} \rangle$ with depth in the upper part of pycnocline (from $\sim$32 m²/s² at $z = 21$ m to $\sim$10 m²/s² at $z = 70$ m) and minor variations of $e_{hf} = 8$–12 m²/s² downward (left panel), but also a temporal variability at all depths. A quasiperiodic increase/decrease of $e_{hf}(z,t)$ in the pycnocline (Figure 9, right panel) indicates the influence of tidal motions on the energy of higher-frequency oscillations. A ratio between the frequency-averaged spectra of zonal and meridional components $\langle S_u/S_v \rangle$ is also shown for several representative depths in Figure 9 (black diamonds in right panel). In the sharp density interface ($z = 29$ m), the energy of zonal fluctuations averaged over a high-frequency band (periods from $\sim$2 h to 9 min) is more than twice the energy of meridional fluctuations; the difference quickly ceased with depth, becoming 1 at $z = 75$ m, generally following the decrease of the total energy $\langle e_{hf} \rangle(z)$ shown in the left panel of Figure 9. Below 75 m, the ratio $\langle S_u/S_v \rangle$ drops to 0.8 at $z = 101$ m, increasing then above 1.5 at $z = 125$ m. The $\langle S_u/S_v \rangle$ ratio and quasiperiodic modulation of the internal wave energy suggest that the generation of high-frequency oscillations in the upper part of the pycnocline may be linked to predominant zonal propagation of internal tide originated near the Andaman Islands [*Wijeratne et al.*, 2010] or at the steep Sri Lankan continental slope [*Prasad and Rajasekhar*, 2011] where the barotropic tides interact with bathymetry.

The above analysis suggests that major spectral maxima in Figures 8a and 8b (τ_{max} varying from $\sim$10 to $\sim$40 min) are stipulated by an ensemble of internal waves. The vertical displacements akin to the internal-wavefield and potential energy of the waves at $z_0 \sim 54$ m are examined next, based on a 20 h time series of 41 profiles ($z = 0$–150 m), the time series recorded at z_0, and continuously sampled (every 30 s, 1 m vertical resolution) backscatter biosonic data.

4.2. Backscatter Spectra

The depth-time variation of normalized backscatter signal $-B_n = Bs/(-Bs_{max})$ is shown in Figure 10 for the last 16 h of continuous operation at the sampling site. The data depict the attenuation of signal at different depths, with lower values of $-B_n$ indicating a higher strength of the signal (warmer colors in the plot). Note that $-B_n$ substantially increased at all depths between $t = 11$ and $t = 13$ h simultaneously with the increase in the flow magnitude $|U|(z, t)$, specifically this applies to the northern component $v(z, t)$ shown in Figure 7. This points to the advective nature of the mesoscale spatial inhomogeneity of biological matter concentration in the area, as alluded to in the discussion of the Sri Lanka Dome, which affects the strength of the backscatter signal. One of the most striking features in Figure 10 is the high-frequency oscillations of $-B_n(z,t)$ that spans the entire pycnocline and is clearly distinguishable during the second half of the observational period, starting from $t \sim 13$ h.
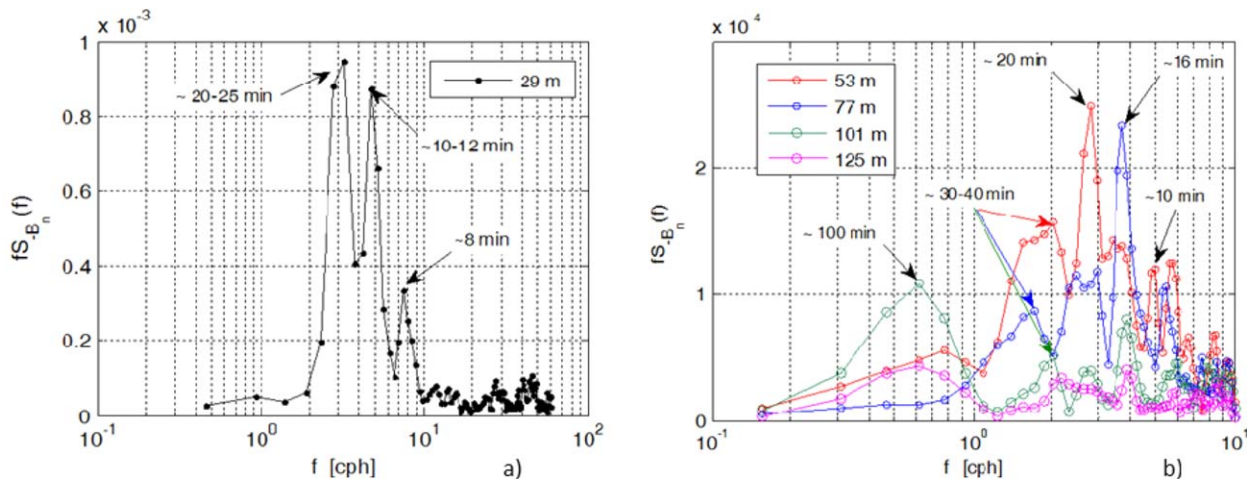
Figure 11. The variance-preserving spectra of the normalized backscatter signal in the middle of a sharp density interface (a) and at several representative depths in the pycnocline (b). In Figure 11b the reduced sampling frequency $\Delta f = 20$ cph was implemented to match that of the kinetic energy spectra given in Figure 8a.

While the major spectral maxima in Figures 8 and 11 do not match exactly, they do closely overlap, suggesting that the periodic oscillations in horizontal ($u(z, t)$ and $v(z, t)$) and vertical $-B_n(z, t)$ directions must be of the internal-wave origin. The characteristic periods τ_{iw} of these internal waves are 10–11, 16–17, 20, 25, 30–40 min, and ~1.5 h. The backscatter signal, however, does not exhibit distinct segments that could be associated with trains of nonlinear waves at a specific phase of tidal flow [*Lee et al.*, 2006; *Lozovatsky et al.*, 2015] or triggered by energetic internal tides [e.g., *Lien et al.*, 2005; *Alford et al.*, 2010; *Li and Farmer*, 2011]. The amplitudes of higher-frequency oscillations in Figure 10 are generally time-dependent, but during relatively long periods they remain quasi-stationary, which is evident from the excursions of the sharp density interface below the mixed layer (the mid-depth 25–30 m) for $t \sim 14$–20 h (Figure 10). The $fS_{-B_n}(f)$ at the interface ($z = 29$ m) calculated with high resolution for this time segment (Figure 11a) contains two narrow energetic maxima corresponding to $\tau_{iw} = 20$–25 and 10–12 min and a lower amplitude $\tau_{iw} \sim 8$ min maximum. Thus, the internal wavefield in the upper pycnocline consists of the major quasi-linear harmonic ($\tau_{iw} = 25$ min) and two consecutive subharmonics.

The baroclinic modal structure of the internal wavefield was examined by solving the Taylor-Goldstein equation [*Smyth et al.*, 2011] for the observed mean buoyancy and velocity profiles (http://roach.coas.ore-gonstate.edu/wave_analysis/SSF_index.html). Since the measurements below 150 m were limited (a deep CTD cast and an averaged velocity profile obtained as a combination of 150 and 75 kHz ADCP data), the computational domain was set up with the lower boundary at 700 m. Below this depth the internal wave activity is assumed to be very low compared to the upper layers (vertical velocity $W(z) = 0$ at $z = 0$ and 700 m). The calculations indicated that quasi-harmonic waves in the very sharp pycnocline between 25 and 40 m (density interface) is linked to the second, third and to a lesser extent to the fourth and fifth vertical modes (not shown), which depict distinct maxima in this depth range. The amplitude of the first vertical mode at the interface is low, comparable to that of the fifth mode. The estimated phase speed of interfacial modes 3–5 are $c_{ph} = 1.0$, 0.78, and 0.64 m/s, respectively, leading to the wavelengths $\lambda = c_{ph}\tau_{iw}$ in the range 1.2–1.5 to 0.4–0.5 km for periods $\tau_{iw} = 20$–25 min and $\tau_{iw} = 10$–12 min (Figure 11a). The second vertical mode, which peaks slightly below the density interface at $z \sim 40$ m, showed $c_{ph} = 1.4$ m/s, and thus the wavelength of a 20 min period waves is about 1.7 km. Notwithstanding the uncertainty of calculations, the above estimates of wave characteristics seem reasonable. More detailed measurements at greater depth are needed to substantiate the modal structure of internal waves in the southern BoB.

4.3. Vertical Displacements: Probability Distribution

Because the mean vertical concentration gradient of the biological matter does not follow the mean density stratification (alternative signs of the $(-\bar{B}_n)_z$ gradient in different layers), it is not feasible to estimate the vertical displacements ζ induced by internal waves using the traditional approach $\zeta(z, t) = \rho'/\bar{\rho}_z$, with ρ' replaced by $-B'_n$ and $\bar{\rho}_z$ by $(-\bar{B}_n)_z$. Thus, we used the time series records at $z_0 = 54$ m and the corresponding vertical profiles of density $\bar{\rho}(z, t)$ to calculate $\rho'(z_0, t)$ and $\bar{\rho}_z(z_0, t)$ in the proximity of z_0. The $\zeta(z_0, t)$
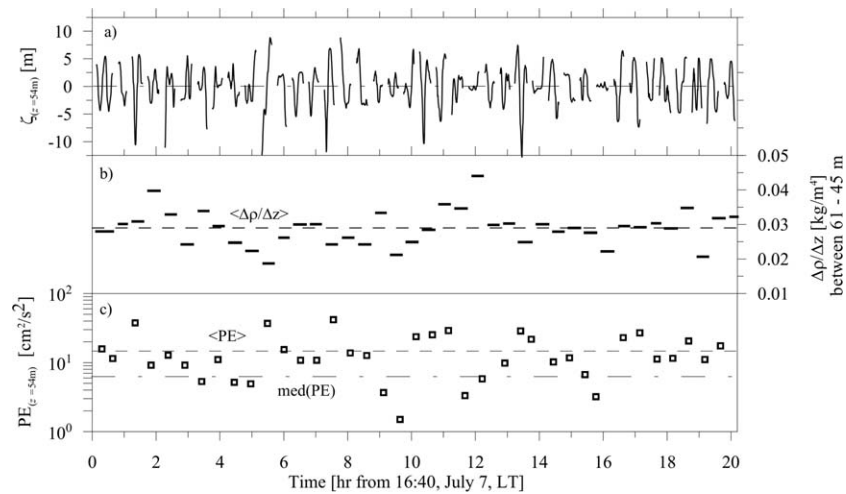
Figure 12. The estimates of vertical displacements ζ (a), the density gradient $\Delta\rho/\Delta z_{(61-45m)}$ between $z = 61$ and 45 m (b), and potential energy of internal waves PE (c) at $z_0 = 54$ m.

displacements (Figure 12a) were obtained using a 20 s averaged and resampled time series of $\rho'_{(i)}(z_0, t) = \rho_i(z_0, t) - \bar{\rho}_i(z_0, t_{(i)})$ along with a density gradient evaluated as $\bar{\rho}_{z(i)} = [\bar{\rho}_i(z_2) - \bar{\rho}_i(z_1)]/(z_2 - z_1)$, where $z_1 = 45$ m and $z_2 = 61$ m surrounding z_0, and coinciding with the closest ADCP bins; $i = 1–41$ is a time series number. The $\bar{\rho}_{z(i)}$ values vary in time in a relatively narrow range, ~ -0.02 to ~ -0.04 kg/m⁴; its mean value $\langle \Delta\rho/\Delta z \rangle = -0.029$ kg/m⁴ is depicted in Figure 12b by the dashed line. The obtained estimates of $\zeta(z_0, t)$ and $\bar{\rho}_{z(i)}$ allowed calculations of the potential energy of internal waves at z_0, namely $PE(z_0, t) = 0.5N_i^2\zeta^2$, where $N_i^2 = (g/\bar{\rho}_{z_0})\bar{\rho}_{z(i)}$ and g is the gravitational acceleration. According to Figure 12c, the potential energy of vertical displacements varied in time by an order of magnitude; the mean and the median estimates for this time period are $\langle PE \rangle = 14.7$ cm²/s² and $med(PE) = 6.3$ cm²/s², respectively. Thus, the ratio between the mean potential (Figure 12c) and kinetic (Figure 11a) energies at z_0 is 14.7/19.6 = 0.75.

By and large, $\zeta(z_0, t)$ does not exceed $\sim \pm$ 5–6 m, but six events where negative $\zeta(z_0, t)$ exceeded 10 m for a short time can be seen in Figure 12a and their appearances are regular with a period of ~ 1 to ~ 3 h. As such, one may speculate that the basic internal wavefield in the southern BoB pycnocline is episodically disturbed by solitary waves of depression.

To better understand statistical properties of internal waves in the upper pycnocline of the southern BoB, we analyzed the probability distribution of vertical displacements ζ at $z_0 = 54$ m. The cumulative distribution function of ζ_{z_0} is shown in Figure 13a, was approximated by the Gaussian (normal) distribution (the straight line in the probability scale) with the nearly zero estimated mean of $\langle \zeta \rangle_n = 6.2 \times 10^{-10}$ m, and the standard deviation of $std(\zeta)_n = 3.34 \pm 0.05$ m. The empirical data follow the Gaussian model for the internal wave amplitudes [*Briscoe*, 1994] very well in the range of probability between 0.05 and 0.95 (the displacement range is ± 6 m) while the tails of the distribution deviate from the normal law. The influence of relatively rare appearance of high-amplitude nonlinear internal wave episodes [e.g., *Lee et al.*, 2006; *Lozovatsky et al.*, 2015] could be a reason why the tails of ζ_{z_0} distribution deviate from normality.

The distribution of the heights of internal waves was less studied compared to the wave amplitudes, but it is important for applications in the same manner as the heights of surface waves. Because we are analyzing the vertical displacements ζ_{z_0} for 40 relatively short segments that usually embrace not more than one-two wave periods, it is not trivial to determine the wave height. Thus, we used the absolute values $|\zeta|$ as a proxy of half of the wave height. It has been noted [e.g., *Forristall*, 1978; *Prevosto et al.*, 2000; *Guedes Soares and Carvalho*, 2001] that the probability distribution of the wave heights for surface waves, which contains double spectral maxima, is more complex than the classical Rayleigh distribution proposed by *Longuet-Higgins* [1952] for one-peaked wave spectra. In our case, $fS|\zeta|(f)$ shown in Figure 13c contains two fairly well-resolved maxima at frequencies $f_{p2} = 0.3$ cph and $f_{p1} = 0.6$ cph (periods ~ 20 and 10 min), portraying at least two ensembles of quasi-harmonic internal waves. The probability functions for $|\zeta|$ in this case can be specified based on the inter-modal distance [*Guedes Soares*, 1984] $IMD = (f_{p2} - f_{p1})/(f_{p2} + f_{p1})$. If IMD tends to
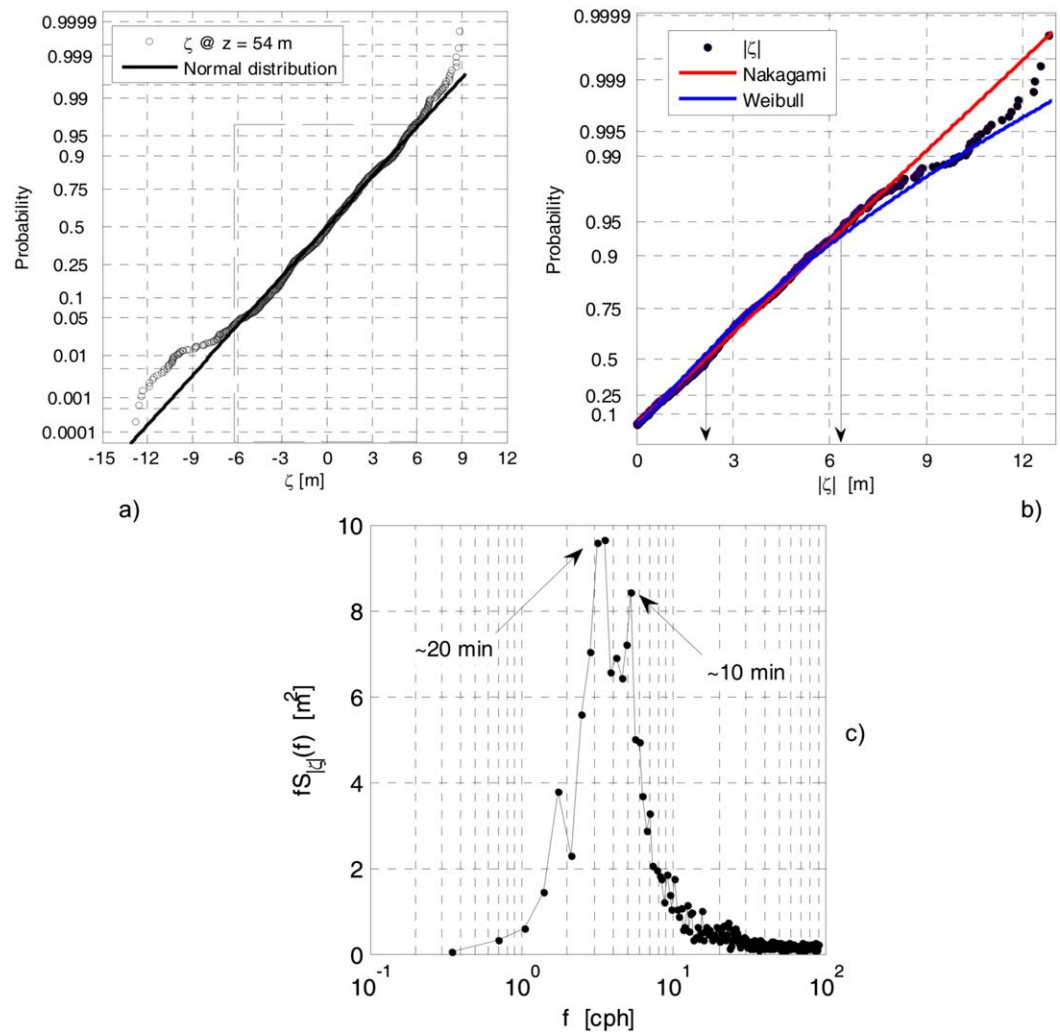
Figure 13. Cumulative distribution function of (a) vertical displacements ζ (IW amplitudes) and (b) their absolute values $|\zeta|$ (IW heights) at $z_0 = 54$ m approximated by a (a) Gaussian and the (b) Weibull and Nakagami models. The dashed box in Figure 13a indicates the [0.05–0.95] distribution range. The variance preserving spectrum of $|\zeta|$ at z_0 is in Figure 13c.

zero, then the classic Rayleigh distribution is expected. For the relatively large *IMD*, such as 0.33 in our case, the Weibull as well as several other models [e.g., *Naess*, 1985] have been suggested [*Guedes Soares and Carvalho*, 2001].

The Weibull [1951] probability distribution function (pdf)

$$pdf_{wb}(x|a_w, c_w) = \frac{c_w}{a_w}\left(\frac{x}{a_w}\right)^{c_w-1} exp\left[-\left(\frac{x}{a_w}\right)^{c_w}\right] \tag{1}$$

is specified by the scale a_w and shape c_w parameters; $x \equiv |\zeta|$. The Weibull cumulative distribution is shown in Figure 13b fitting the empirical absolute displacements $|\zeta|$ with $a_w = 2.74 \pm 0.05$ m and $c_w = 1.18 \pm 0.02$ (the mean and the median $|\zeta|$ are 2.6 and 2.1 m, respectively, and the $rms(|\zeta|) = 2.2$ m). The Weibull distribution as well as its relative, the Rayleigh distribution, has been previously applied to a statistical analysis of surface waves heights [e.g., *Longuet-Higgins*, 1980; *Guedes Soares and Carvalho*, 2001; *Wang and Gao*, 2002] and for the other oceanographic variables [e.g., *Lozovatsky and Erofeev*, 1993; *Planella et al.*, 2011]. The Weibull model fits ~90% of the empirical data (see Figure 13b, $|\zeta| < 6$ m), while the Nakagami distribution,

$$pdf_{nk}(x|a_{nk}, m) = \frac{2}{\Gamma(m)}\left(\frac{m}{a_{nk}}\right)^m x^{2m-1} exp\left(-\frac{m}{a_{nk}}x^2\right), \tag{2}$$

which is from the same family of distributions as the Weibull, embraces almost 98% of the data set; $\Gamma(m)$ is a gamma function. The absolute values of vertical displacements associated with high-frequency waves followed the Nakagami distribution within a 95% quintile of 6.5 m. Only for very large displacements ($|\zeta| > 8$ m) the empirical distribution in Figure 13b deviates from the Nakagami straight line, specified by the scale parameter $a_{nk} = 11.17 \pm 0.34$ m and the shape parameter $m = 0.455 \pm 0.011$. Note that Nakagami distribution successfully models the probability functions of attenuating amplitude of scattering signals traversing from different directions. Thus, it is reasonable to suggest that ∼98% of the internal waves observed were generated at various distances from the measurement site and were scattered within the intermittently turbulent upper pycnocline during the course of their propagation. The largest waves, $8 < |\zeta| < 13$ m, which constitute only 2% of the data set, are probably rare solitary waves that propagate through the intermittently turbulent pycnocline with weak scattering.

4.4. Shear Instability in the Lower Part of the Upper Pycnocline

Statistical analysis of vertical displacement in the upper pycnocline ($z_0 = 54$ m), wherein stable stratification is strong, suggests remote generation of internal waves, which are scattered before arriving at the measurement location. The contour plot of Richardson number $Ri = N^2/Sh^2$ shown in Figure 14 (lower) supports this assumption. Here N^2 and Sh^2 the squared buoyancy frequency and squared shear calculated, respectively, based on the SeaBird and HDSS data with 3 m vertical resolution. At the depth, $z_0 = 54$ m (marked in Figure 14 by the dashed line), the Richardson number exceeds unity most of the time, showing low probability of shear instability that has a propensity to generate internal waves locally. However, deeper in the pycnocline, several clusters $Ri < 1$ or even $Ri < 0.25$ patches are observed, mainly between 90 and 130 m (encircled by ellipses in the Ri contour plot). The same ellipses are superpositioned on the Ellison scale plot (Figure 14, upper), which shows that three out of four ellipses embraced patches of high L_E. In one case (the dashed line ellipse), relatively low Ri are not associated with elevated L_E. Note that the Ellison scale $L_E = (\rho - \tilde{\rho})/\tilde{\rho}_z$ was estimated using the "undisturbed" density profiles $\tilde{\rho}(z)$ obtained by a 7-point moving-average of the original $\rho(z)$ profiles. This is one of the traditional approaches [*Fedorov*, 1978] to extract the fine structure using density profiles. Sans thermohaline intrusions (our case), the Ellison scale is usually associated with the amplitude of linear internal waves, and to a lesser extent with the characteristic sizes of the pycnocline layer structure (double diffusive layering, turbulent patches). Figure 14 indicates that below z ∼75–90 m, high-amplitude internal waves ($L_E > \sim 4$ m) could be generated locally due to episodic development of instability associated with relatively low Richardson numbers.

To estimate the probability of Ri to become subcritical, i.e., $Ri < Ri_{cr}$, where the value of Ri_{cr} depends on the type of instability, the cumulative distribution functions $CDF(Ri^{-1})$ of the inverse Richardson number Ri^{-1}
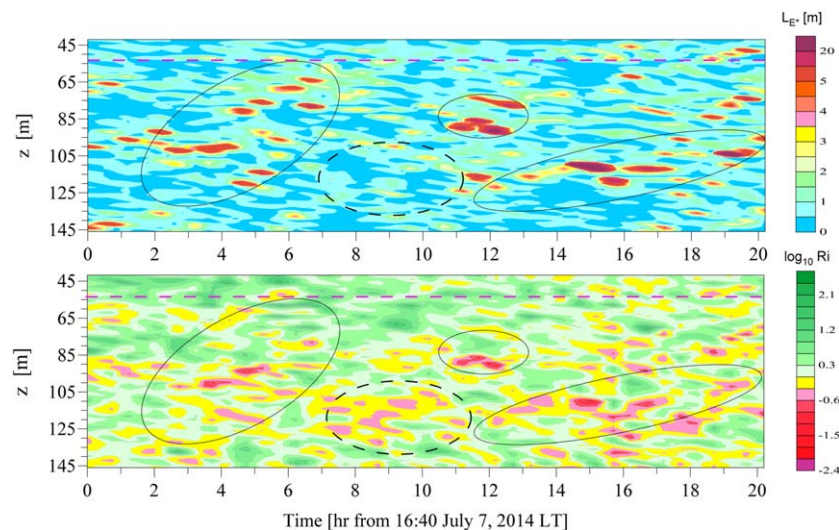

Figure 14. The contour plots of the Ellison scale L_{E^*} (upper) and the logarithm of Richardson number $\log_{10} Ri$ (lower figure); z_0 is marked in $L_{E^*}(z,t)$ and $\log_{10} Ri(z,t)$ plots by the dashed magenta lines. Three clusters of patches with enhanced L_{E^*} are encircled by continuous ellipses and these ellipses are copied to the $\log_{10} Ri$ plot, depicting patches of small Ri (often bellow critical). The dashed ellipses in both figures indicate the case when patches of the near critical Ri do not excite the increase of L_{E^*}
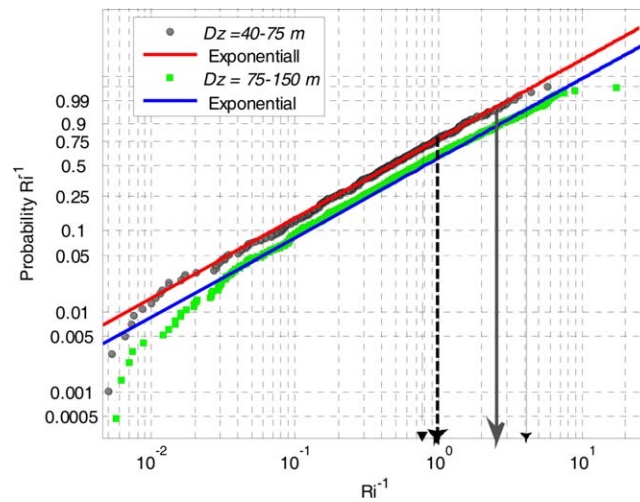
Figure 15. Cumulative distribution functions of the inverse Richardson number Ri^{-1} for two depth ranges in the pycnocline approximated by exponential distributions. The critical $Ri^{-1} > Ri_{cr}^{-1} = 2.8$ for billows is shown by a solid bold line arrow; for asymmetric waves $Ri_{cr}^{-1} = 1$ by a dashed bold line and for the Holmboe waves $Ri^{-1} > Ri_{cr}^{-1} = 0.77$ by a dashed-dotted line. The critical $Ri^{-1} > Ri_{cr}^{-1} = 4$ for shear-generated turbulence is marked by a thin solid arrow.

were calculated separately for the depth ranges $Dz = 40–75$ and $Dz = 75–150$ m. As discussed in section 3, the flow above $z \sim 75$ m is northeastward, while below this level the flow episodically ($t = 4–6$ h and $t = 13–9$ h) turns northwestward. The empirical $CDF(Ri^{-1})$ are shown in Figure 15, where they are in excellent agreement with the following CDF of simple exponential distribution:

$$CDF(x, \mu) = 1 - e^{-x/\mu}, \; x \geq 0, \quad (3)$$

where $x = Ri^{-1}$, μ is the mean, and μ^2 is the variance. The parameter μ is $\mu_{(40-75)} = 0.67 \pm 0.03$ for Ri^{-1} in the depth range $Dz = 40–75$ and $\mu_{(75-150)} = 1.16 \pm 0.035$ for Ri^{-1} in the range $Dz = 75–150$ m. The exponential distribution of Ri^{-1} has been already utilized by *Anderson* [1992] and *Polzin* [1992] (unpublished manuscripts referred to by *Pinkel and Anderson* [1997]). The behavior

of (3) is similar to a probability distribution for Ri^{-1} suggested by *Pinkel and Anderson* [1997]. Because equation (3) describes the distribution of times or distances between random events subjected to Poison distribution (for example, the generation of turbulence or internal waves in our case), it is possible to interpret Ri^{-1} as a random waiting time needed to achieve a specific critical value $Ri^{-1} = Ri_{cr}^{-1}$.

Based on laboratory results of internal wave generation at a sheared density interface [*Strang and Fernando*, 2001a] and their application to oceanic pycnocline [*Strang and Fernando*, 2001b; *Lee et al.*, 2006], the following criteria have been offered for various types of instabilities: (i) when $Ri < 0.36$, Kelvin-Helmholtz (K-H) billows are generated; (ii) when Ri is in the range between 0.36 and 1, a resonant combination of K-H billows and asymmetric waves occurs; (iii) the K-H instabilities disappear when $Ri \rightarrow Ri_{cr} = 1$; (iv) asymmetric breaking internal waves prevail when $1 < Ri < 1.3$, and (v) for $Ri > 1.3$, Holmboe waves dominate in the pycnocline. Casting these findings in terms of Ri^{-1} and adopting a $CDF(Ri^{-1})$ as shown in Figure 15, it is possible to conclude that for a northeastward flow the probability of developing K-H billows, $Ri^{-1} > 2.8$ ($Ri < 0.36$), is less than 4% and for the northwestward flow below 75 m it is less than 10%. However, the probability of generating breaking waves ($1 > Ri^{-1} > 0.77$) is much higher: it is close to 25–30% for $Dz = 40–75$ m and about 40–50% for $Dz = 75–150$ m. The Holmboe waves ($Ri^{-1} > 0.77$) have the highest probability to exist in the southern BoB pycnocline. Thus, the local generation of billows in the southern BoB pycnocline by K-H instability, which is signified by $Ri < Ri_{cr} = 0.36$, can be considered as a series of sporadic events, while the generation of Holmboe internal waves is much more frequent, approaching in some layers probability of 50%. Note that the classical criterion based on the linear stability theory $Ri^{-1} > 4$ ($Ri < 0.25$) for shear-induced turbulence is satified only for 1 and 4% of the Ri samples above and below $z = 75$ m, respectively. The generation of turbulence by convective instability of internal waves, which requires $Ri^{-1} > 1$, is a much more feasible process having more than 25% of probability to be realized. Note that all parameters related to the Ri^{-1} distributions are valid only for Ri calculated within a 3 m vertical separation distance.

5. Summary

A 20 h time series of CTD, ADCP, and acoustic backscatter profiles down to 150 m, and temporal CTD measurements at $z_0 = 54$ m in between the CTD profiles, were taken at the northeastern periphery of the Sri Lanka Dome (SLD), as determined by a composite analysis of satellite images and drifter trajectories. The observed transport of more saline, slightly cooler waters in the surface layer could be attributed to the circulation associated with SLD that has been already developed in the region at the end of June in response to

cyclonic curl of the local wind field stress. At the beginning of July, the SLD was found to stretch along a northeast-southwest axis, at the same time moving slightly to the west.

During the observational period, the surface mixed-layer depth ranged between ∼19 and 33 m. The MLD was influenced by air-sea interactions [*Parampil et al.* 2010] as well as higher-frequency internal waves in the underlying sharp narrow pycnocline. Quasiperiodic oscillations of the MLD are well-correlated with internal-wave displacements of the upper halocline, specifically during the daytime where the sea surface fluxes do not change as much. The estimated height of low-frequency linear internal waves, which heaves the entire pycnocline, is ∼16 m. The advection of higher salinity waters near the sea surface by northeastward currents causes the former to spread over the entire mixed layer. The thermohaline structure at all depths below the upper mixed layer is embedded within the internal-wave perturbations, causing relatively wide scatter of the vertical (z) thermohaline profiles. The scatter essentially vanishes when T and S are plotted as a function of the potential density [$T(\rho_\theta)$ and $S(\rho_\theta)$].

The depth-time variation of velocity components indicates a multilayered structure of the mean currents. It appears that the strong northeastward surface current identified by drifter trajectories is confined to the upper mixed layer. In the narrow density interface (between ∼25–30 and 40 m), the current magnitude is much weaker (about 10 cm/s) than that in the mixed layer. The flow even exhibits a northwestward component and continues to be influenced by anticyclonic circulation of the SLD. The upper part of the main pycnocline ($z \sim 50$–80 m) is occupied by the strongest northeastward flow (∼25–35 cm/s). Below 80 m, the flow is weaker (∼10–15 cm/s), often highlighting the westward component, which is a part of the anticyclonic circulation.

The depth-averaged magnitudes of horizontal velocity components $\langle u \rangle(t)$ and $\langle v \rangle(t)$ point to the tidal origin of the low-frequency currents, which is consistent with the notion that the largest vertical displacement of the pycnocline is due to internal tides with a predominant semidiurnal period. The internal-wave origin of the well-identified higher-frequency oscillations of the horizontal velocity is clearly supported by the backscatter signal.

Quasi-harmonic internal waves with periods from ∼10 to 40 min are registered at all depths below a shallow surface mixed layer in the background of a 16 m height internal tide. The periodic (about every 6 h) increase/decrease of the kinetic energy of internal waves indicates their link to tidal motions. The changes in stratification and currents associated with moving SLD may have an impact on the baroclinic internal tide, but the effect of these changes ought to be small for highest-frequency waves. The vertical displacements at $z_0 = 54$ m ζ_{z_0} are predominantly less than ±5–6 m, however, several recurring short-lived events with negative displacements exceeding 10 m are also observed. It seems that the basic quasi-harmonic internal wavefield in the southern BoB pycnocline is episodically disturbed by solitary waves of depression.

The probability distribution of vertical displacements ζ_{z_0} of high-frequency waves is Gaussian in the probability range from 0.05 to 0.95. The tails of the distribution are affected by rare appearance of high-amplitudes waves. The distribution of wave heights expressed through the absolute values of $|\zeta_{z_0}|$ are modeled by using Weibull and Nakagami distributions. The Weibull model fits ∼90% of the empirical data, while the Nakagami distribution follows ∼98% of the data set. Based on characteristic processes that lead to Nakagami distribution, it is possible to suggest that the majority of internal waves observed in the upper part of a strong pycnocline are generated away from the measurement location and scattered during their propagation in the intermittently turbulent upper pycnocline.

At the same time, sporadic appearances of high-amplitude vertical displacements (the Ellison scale >4–5 m) in the lower portion of the pycnocline often coincide with patches of low Richardson numbers, pointing to local shear instability as a possible mechanism of internal wave generation, although these are rare events. Based on the probability distribution of the inverse Richardson number Ri^{-1}, which follows the exponential distribution exceedingly well, the appearance of shear instability in the summer BoB pycnocline is relatively low and do not exceed 4–10% for $Ri < 0.36$ (generation of K-H billows). The generation of asymmetric breaking internal waves ($Ri < 1.3$) and Holmboe waves, however, more probable, exceeds 25% in the pycnocline above $z = 75$ m and approaches 40–50% in deeper layers. Note that the classical criterion $Ri^{-1} > 4$ ($Ri < 0.25$) for shear-induced turbulence is satisfied with a probability of ∼1 and 4%, respectively, for Ri samples above and below $z = 75$ m. Results from previous studies [e.g., *Pinkel and Anderson*, 1997] and current analysis suggest that the simple exponential probability distribution can model the distribution of Ri^{-1}

in an ocean pycnocline affected by instabilities of internal waves and mean shear. The probability of each specific type of instability is expected to vary depending on stratification and local dynamics.

Although limited in scope, this study portrays the dynamic nature of the Sri Lanka Dome, which appears to be frequently perturbed by small-scale internal waves embedded in the semidiurnal tide while exhibiting intermittent strong shear in the pycnocline. The measurements were conducted in the middle of the summer, and hence conclusions are valid for this specific region and the summer monsoon season. The horizontal inhomogenity and seasonal dependence of the BoB oceanography calls for more regional studies spanning over more than one season [*Benshila et al.*, 2014], and various components of the ASIRI-EBoB program address such issues.

References

Alford, M. H., R.-C. Lien, H. Simmons, J. Klymak, S. Ramp, Y. J. Yang, D. Tang, and M.-H. Chang (2010), Speed and evolution of nonlinear internal waves transiting the South China Sea, *J. Phys. Oceanogr.*, *40*, 1338–1355.

Anderson, S. A. (1992), Shear, strain, and thermohaline vertical fine structure in the upper ocean, Ph.D. thesis, 173 pp., University of California, San Diego, Calif.

Anil Kumar, M. (2015), Impact of the cold water band and the Sri Lanka Dome on the biogenic fluxes in the Southern Bay of Bengal, *Int. J. Innovative Sci. Eng. Technol.*, *2*(8), 163–179.

Balk, H., and T. Lindem (2007), *Sonar 4 and Sonar 5-Pro Post Processing Systems, Operator Manual*, version 5.9.7., Balk and Lindem Ltd., Oslo, Norway.

Benshila, R., F. Durand, S. Masson, R. Bourdallé-Badie, C. de Boyer Montégut, F. Papa, and G. Madec (2014), The upper Bay of Bengal salinity structure in a high-resolution model, *Ocean Modell.*, *74*, 36–52.

BioSonics. (2004), *EcoSAV^TM: Users Guide*. 17 pp., BioSonics, Inc., Seattle, Wash. [Available at http://www.biosonicsinc.com.]

Briscoe, M. G. (1977), Gaussianity of internal waves, *J. Geophys. Res.*, *82*(15), 2117–2126.

Depew, D. C., A. W. Stevens, R. E. H. Smith, and R. E. Hecky (2009), Detection and characterization of benthic filamentous algal stands (Cladophora sp.) on rocky substrata using a high-frequency echosounder, *Limnol. Oceanogr. Methods*, *7*, 693–705.

de Vos, A., C. B. Pattiaratchi, and E. M. S. Wijeratne (2014), Surface circulation and upwelling patterns around Sri Lanka, *Biogeosciences*, *11*, 5909–5930, doi:10.5194/bg-11-5909-2014.

Egbert, G. D., and S. Y. Erofeeva (2002), Efficient inverse modeling of barotropic ocean tides, *J. Atmos. Oceanic Technol.*, *19*(2), 183–204.

Fedorov, K. N. (1978), *The Thermohaline Finestructure of the Ocean, Pergamon Mar. Ser.*, vol. 2, 170 p., Oxford, Pergamon Press.

Forristall, G. Z. (1978), On the statistical distribution of wave heights in a storm, *J. Geophys. Res.*, *83*(C5), 2353–2358.

Guedes Soares, C. (1984), Representation of double-peaked sea wave spectra, *Ocean Eng.*, *11*, 185–207.

Guedes Soares, C., and A. N. Carvalho (2001), Probability distributions of wave heights and periods in measured two-peaked spectra from the Portuguese coast, in *Proceedings of OMAE'01, 20th International Conference on Offshore Mechanics and Arctic Engineering*, ASME, New York.

Jackson, C. R. (2004), An atlas of internal solitary-like waves and their properties, 2nd ed. [Available at www.internalwaveatlas.com/Atlas2_index.html.]

Jackson, C. R. (2009), Investigation into the character and worldwide distribution of internal solitary waves. [Available at http://www.internalwaveatlas.com.]

Jensen, T. G. (2001), Arabian Sea and Bay of Bengal exchange of salt and tracers in an ocean model, *Geophys. Res. Lett.*, *28*(20), 3967–3970.

Lee J.-H., I. D. Lozovatsky, S.-T. Jang, C.-J. Jang, C.-S. Hong, and H. J. S. Fernando (2006), Episodes of nonlinear internal waves in the Northern East China Sea, *Geophys. Res. Lett.*, *33*, L18601, doi:10.1029/2006GL027136.

Li, Q., and D. M. Farmer (2011), The generation and evolution of nonlinear internal waves in the deep basin of the South China Sea, *J. Phys. Oceanogr.*, *41*, 1345–1363, doi:10.1175/2011JPO4587.1.

Lien, R.-C., T. Y. Tang, M. H. Chang, and E. A. D'Asaro (2005), Energy of nonlinear internal waves in the South China Sea, *Geophys. Res. Lett.*, *33*, L05615, doi:10.1029/2004GL022012.

Longuet-Higgins, M. S. (1952), On the statistical distribution of the heights of sea waves, *J. Mar. Res.*, *11*, 1245–1266.

Longuet-Higgins, M. S. (1980), On the distribution of heights of sea waves: Some effects of nonlinearity and finite bandwidth, *J. Geophys. Res.*, *85*(C3), 1519–1523.

Lozovatsky, I. D., and A. Y. Erofeev (1993), Statistical approach to eddy viscosity simulation for numerical models of the upper turbulent layer, *J. Mar. Syst.*, *4*, 391–399, doi:10.1016/0924-7963(93)90023-F.

Lozovatsky, I., S. U. P. Jinadasa, J.-H. Lee, and H. J. S. Fernando (2015), Internal waves in a summer pycnocline of the East China Sea, *Ocean Dyn.*, *65*(8), 1051–1061, doi:10.1007/s10236-015-0858-2.

Lucas, A. J., et al. (2014), Mixing to monsoons: Air-Sea interactions in the Bay of Bengal, *Eos Trans. AGU*, *95*(30), 269–270.

Lumpkin, R., and M. Pazos (2007), Measuring surface currents with surface velocity program drifters: The instrument, its data, and some recent results, in *Lagrangian Analysis and Predictability of Coastal and Ocean Dynamics*, edited by A. Griffa et al., pp. 39–67, Cambridge Univ. Press, Cambridge, U. K.

Maury, M. F. (1861), *The Physical Geography of the Sea and its Meteorology*, 405 pp., Harper, N. Y.

Naess, A. (1985), On the distribution of crest to trough wave heights, *Ocean Eng.*, *12*(3), 221–234.

Osborne, A. R., and T. L. Burch (1980), Internal solitons in the Andaman Sea, *Science*, *208*, 451–460.

Parampil, S. R., A. Gera, M. Ravichandran, and D. Sengupta (2010), Intraseasonal response of mixed layer temperature and salinity in the Bay of Bengal to heat and freshwater flux, *J. Geophys. Res.*, *115*, C05002, doi:10.1029/2009JC005790.

Pinkel, R., and S. Anderson (1997), Shear, strain, and Richardson number variations in the thermocline. Part I: Statistical description, *J. Phys. Oceanogr.*, *27*, 264–281.

Pinkel, R., L. Rainville, E. Slater, A. Goldin, L. Green, M. Bui, and T. Aja (2003), The hydrographic Doppler sonar system on the Roger Revelle, in *Proceedings of the IEEE/OES Seventh Working Conference on Current Measurement Technology*, pp. 237–239, doi:10.1109/CCM.2003.1194320.

Planella, J., E. Roget, and I. Lozovatsky (2011), Statistics of microstructure patchiness in a stratified lake, *J. Geophys. Res.*, *116*, C10035, doi: 10.1029/2010JC006911.

Polzin, K. L. (1992), Observations of turbulence, internal waves, and background flows: An inquiry into the relationship between scales of motion, MIT/WHOI, WHOI-92-39, Woods Hole Oceanographic Institution, 243 pp.

Prasad, K. V. S. R., and M. Rajasekhar (2011), Space borne SAR observations of oceanic internal waves in North Bay of Bengal, *Nat. Hazards*, *57*, 657–667.

Prevosto, M., H. E. Krogstad, and A. Robin (2000), Probability distributions for maximum wave and crest heights, *Coastal Eng.*, *40*, 329–360.

Rainville, L., and R. Pinkel (2004), Observations of energetic high-wavenumber internal waves in the Kuroshio, *J. Phys. Oceanogr.*, *34*, 1495–1505.

Rao, A. D, S. V. Babu, K. V. S. R. Prasad, T. V. R. Murty, Y. Sadhuram, and D. K. Mahapatra (2010), Investigation of the generation and propagation of low frequency internal waves: A case study for the east coast of India, *Estuarine Coastal Shelf Sci.*, *88*, 143–152.

Rudstam, L. G., S. L. Parker-Stetter, P. J. Sullivan, and D. M. Warner (2009), Towards a standard operating procedure for fishery acoustic surveys in the Laurentian Great Lakes, North America, *ICES J. Mar. Sci.*, *66*, 1391–1397.

Smyth, W. D., P. O. Zavialov, and J. N. Moum (1997), Decay of turbulence in the upper ocean following sudden isolation from surface forcing, *J. Phys. Oceanogr.*, *27*, 820–822.

Smyth, W. D., J. N. Moum, and J. D. Nash (2011), Narrowband oscillations in the upper Equatorial Ocean. Part II: Properties of shear instabilities, *J. Phys. Oceanogr.*, *41*, 412–428.

Sridevi, B., T. V. Ramana Murty, Y. Sadhuram, M. M. M. Rao, K. Maneesha, S. Sujith Kumar, and P. L. Prasanna (2010), Impact of internal waves on sound propagation off Bhimilipatnam, east coast of India. *Estuarine Coastal Shelf Sci.*, *88*, 249–259.

Sridevi, B., T. R. Murty, Y. Sadhuram, V. V. S. S. Sarma, V. S. N. Murty, and K. V. S. R. Prasad (2014), Tidally-modulated high frequency internal waves in Gautami-Godavari estuary, East coast of India, *Indian J. Geo-Mar. Sci.*, *43*, 9.

Strang, E. J., and H. J. S. Fernando (2001a), Entrainment and mixing in stratified shear flows, *J. Fluid Mech.*, *428*, 349–386.

Strang, E. J., and H. J. S. Fernando (2001b), Vertical mixing and transport through a stratified shear layer, *J. Phys. Oceanogr*, *31*, 2026–2048.

Vinayachandran, P. N., and T. Yamagata (1998), Monsoon response of the sea around Sri Lanka: Generation of thermal domes and anticyclonic vortices, *J. Phys. Oceanogr.*, *28*, 1946–1960.

Vinayachandran, P. N., D. Shankar, S. Vernekar, K. K. Sandeep, P. Amol, C. P. Neema, and A. Chatterjee (2013), A summer monsoon pump to keep the Bay of Bengal salty, *Geophys. Res. Lett.*, *40*, 1777–1782, doi:10.1002/grl.50274.

Wang, T. and T.-F. Gao (2002), Statistical properties of high-frequency internal waves in Qingdao offshore area of the Yellow Sea, *Chin. J. Ocean Limnol.*, *20*(1), 16–21.

Weibull, W. (1951), A statistical distribution function of wide applicability, *J. Appl. Mech.*, *N9*, 293–297.

Wijeratne, E. M. S., P. L. Woodworth, and D. T. Pugh (2010), Meteorological and internal wave forcing of seiches along the Sri Lanka coast, *J. Geophys. Res.*, *115*, C03014, doi:10.1029/2009JC005673.

Wijesekera, H. W., and M. C. Gregg (1996), Surface layer response to weak winds, westerly bursts, and rain squalls in the western Pacific warm pool, *J. Geophys. Res.*, *101*, 977–997.

Wijesekera, H. W., T. G. Jensen, E. Jarosz, W. J. Teague, E. J. Metzger, D. W. Wang, S. U. P. Jinadasa, K. Arulananthan, L. R. Centurioni, and H. J. S. Fernando (2015), Southern Bay of Bengal currents and salinity intrusions during the northeast monsoon, *J. Geophys. Res. Oceans*, *120*, 6897–6913, doi:10.1002/2015JC010744.